THE ASTROPHYSICAL JOURNAL, 560:659–674, 2001 October 20


# CHARACTERISTIC X-RAY VARIABILITY OF TeV BLAZARS: PROBING THE LINK BETWEEN THE JET AND THE CENTRAL ENGINE

JUN KATAOKA,[1] TADAYUKI TAKAHASHI,[2] STEFAN J. WAGNER,[3] NAOKO IYOMOTO,[2] PHILIP G. EDWARDS,[2] KIYOSHI HAYASHIDA,[4] SUSUMU INOUE,[5] GREG M. MADEJSKI,[6] FUMIO TAKAHARA,[4] CHIHARU TANIHATA,[2] AND NOBUYUKI KAWAI[1]

*Received 2000 June 23; accepted 2001 May 2*

## ABSTRACT

We have studied the rapid X-ray variability of three extragalactic TeV $\gamma$-ray sources: Mrk 421, Mrk 501, and PKS 2155−304. Analyzing the X-ray light curves obtained from *ASCA* and/or *Rossi X-Ray Timing Explorer* observations between 1993 and 1998, we have investigated the variability in the time domain from $10^3$ to $10^8$ s. For all three sources, both the power spectrum density (PSD) and the structure function (SF) show a rollover with a timescale of the order of 1 day or longer, which may be interpreted as the typical timescale of successive flare events. Although the exact shape of turnover is not well constrained and the low-frequency (long timescale) behavior is still unclear, the high-frequency (short timescale) behavior is clearly resolved. We found that, on timescales shorter than 1 day, there is only small power in the variability, as indicated by a steep power spectrum density of $f^{-2\sim-3}$. This is very different from other types of mass-accreting black hole systems, for which the short-timescale variability is well characterized by a fractal, flickering-noise PSD ($f^{-1\sim-2}$). The steep PSD index and the characteristic timescale of flares imply that the X-ray–emitting site in the jet is of limited spatial extent: $D \geq 10^{17}$ cm distant from the base of the jet, which corresponds to $\geq 10^2$ Schwarzschild radii for $10^{7-10}$ $M_\odot$ black hole systems.

*Subject headings:* BL Lacertae objects: general — galaxies: active — X-rays: galaxies

## 1. INTRODUCTION

Observations with the EGRET instrument (30 MeV to 30 GeV; Thompson et al. 1993) on board the *Compton Gamma-Ray Observatory* (*CGRO*) have detected $\gamma$-ray emission from over 60 active galactic nuclei (AGNs; e.g., Hartman et al. 1999). Most of the AGNs detected by EGRET show characteristics of the blazar class of AGNs, such as violent optical flaring, high optical polarization, and flat radio spectra (Angel & Stockman 1980). Observations with ground-based Cherenkov telescopes have detected $\gamma$-ray emission extending up to TeV energies for a number of nearby AGNs. We limit our discussion in this paper to the three TeV sources for which substantial X-ray data sets are available: Mrk 421 ($z = 0.031$; TeV detection reported by Punch et al. 1992), Mrk 501 ($z = 0.034$; Quinn et al. 1996), and PKS 2155−304 ($z = 0.117$; Chadwick et al. 1999).

The overall spectra of blazars (plotted as $\nu F_\nu$) have two pronounced continuum components: one peaking between IR and X-rays and the other in the $\gamma$-ray regime (e.g., von Montigny et al. 1995). The lower energy component is believed to be produced by synchrotron radiation from relativistic electrons in magnetic fields, while inverse Compton scattering by the same electrons is thought to be the dominant process responsible for the high-energy $\gamma$-ray emission (e.g., Ulrich, Maraschi, & Urry 1997). The radiation is emitted from a relativistic jet, pointing close to our line of sight (e.g., Urry & Padovani 1995). VLBI observations of superluminal motions confirm that the jet plasma is moving with Lorentz factors of $\Gamma \simeq 10$ (e.g., Vermeulen & Cohen 1994).

Blazars are commonly variable from radio to $\gamma$-rays. The variability timescale is shortened and the radiation is strongly enhanced by relativistic beaming. For extragalactic TeV sources, the X-ray/TeV $\gamma$-ray bands correspond to the highest energy ends of the synchrotron/inverse Compton emissions, which are produced by electrons accelerated up to the maximum energy (e.g., Inoue & Takahara 1996; Kirk, Rieger, & Mastichiadis 1998; Kusunose, Takahara, & Li 2000). At the highest energy ends, variability is expected to be most pronounced; indeed, multifrequency campaigns of Mrk 421 have reported more rapid and larger amplitude variability in both X-ray and TeV $\gamma$-ray bands than in other wavelengths (e.g., Macomb et al. 1995; Buckley et al. 1996; Takahashi, Madejski, & Kubo 1999; Takahashi et al. 2000). Thus, X-ray variability can be the most direct way to probe the dynamics operating in jet plasma, in particular compact regions of shock acceleration that are presumably close to the central engine.

"Snapshot" multiwavelength spectra principally provide us with clues on the emission mechanisms and physical parameters inside relativistic jets. On the other hand, detailed studies of time variability not only lead to complementary information for the objectives above but also should offer us a more direct window on the physical processes operating in the jet as well as on the dynamics of the jet itself. However, short time coverage and undersampling have prevented detailed temporal studies of blazars. Only a few such studies have been made in the past for blazars, e.g., evaluation of the energy dependent "time lags" based on

[1] Department of Physics, Faculty of Science, Tokyo Institute of Technology, Meguro-ku, Tokyo 152-8551, Japan.
[2] Institute of Space and Astronautical Science, Sagamihara, Kanagawa 229-8510, Japan.
[3] Landessternwarte Heidelberg, Königstuhl, D-69117 Heidelberg, Germany.
[4] Department of Earth and Space Science, Graduate School of Science, Osaka University, Toyonaka, Osaka 560-0043, Japan.
[5] Theoretical Astrophysics Division, National Astronomical Observatory, Mitaka, Tokyo 181-8588, Japan.
[6] Stanford Linear Accelerator Center, 2575 Sand Hill Road, Menlo Park, CA 94025.

the synchrotron cooling picture (e.g., Takahashi et al. 1996, 2000; Kataoka et al. 2000).

Variability studies covering a large dynamic range and a broad span of timescales have become common for Seyfert galaxies and Galactic black holes (e.g., Hayashida et al. 1998; Edelson & Nandra 1999; Chiang et al. 2000). From power spectrum density (PSD) analyses, it is well known that rapid fluctuations with frequency dependences $P(f) \propto f^{-1 \sim -2}$ are characteristic of time variability in accreting black hole systems. Although their physical origin is still under debate, some tentative scenarios have been suggested to account for these generic, fractal features (e.g., Kawaguchi et al. 2000).

Our main goal is to delineate the characteristic time variability of the X-ray emission from TeV $\gamma$-ray sources, highlighting the differences between such *jet-enhanced* objects (blazars) and sources without prominent jets (Seyfert galaxies and Galactic black holes). Very recently, three TeV sources were intensively monitored in the X-ray band (Kataoka 2000; Takahashi et al. 2000), providing valuable information on the temporal behavior of these objects. The most remarkable result is a detection of a clear "rollover" in the structure function (SF; § 2.4) of Mrk 421 in a 1998 observation (Takahashi et al. 2000). Such a rollover, if confirmed, would yield considerable scientific fruits about the physical origin and the location of X-ray emission inside the jet plasma, which is the primary motivation of this paper. Systematic studies using a larger sample of data will be necessary to confirm and unify the variability features in blazars.

Combining data from archival *ASCA* and *Rossi X-Ray Timing Explorer* (*RXTE*) observations over 5 yr (3 yr for *RXTE*), we derive here the variability information on timescales from minutes to years. This is the first report of variability analysis of blazars based on high-quality data covering the longest observation periods available at X-ray energies. The observations and data reduction are described in §§ 2.1 and 2.2. Temporal studies using the PSD are described in § 2.3, while an alternative approach using the SF is considered in § 2.4. In § 3, we discuss the origin of the rapid variability. Finally, in § 4 we present our conclusions.

## 2. TEMPORAL ANALYSIS

### 2.1. *Observations*

The three extragalactic TeV sources were observed a number of times with the X-ray satellites *ASCA* and/or *RXTE*. Observation logs are given in Tables 1 and 2. *ASCA* observed Mrk 421 five times with a net exposure of 546 ks between 1993 and 1998. In the 1998 observation, the source was in a very active state and was detected at its highest ever level (Takahashi et al. 2000). *RXTE* observed Mrk 501 more than 100 times with a net exposure of 700 ks between 1996 and 1998. Mrk 501 was in a historical high state in 1997 (Catanese et al. 1997; Pian et al. 1998; Lamer & Wagner 1998). Multiwavelength campaigns, including a number of target-of-opportunity observations, were conducted during this high state. PKS 2155−304 was observed with *ASCA* for 133 ks in 1993–1994, while observations over 246 ks were conducted with *RXTE* in 1996–1998. Full descriptions of the *ASCA* and *RXTE* monitorings of TeV sources, other than those observations discussed in this paper, are given in Kataoka (2000). In the following, we classify the X-ray observations into two convenient groups based on their sampling strategy.

The first group is the *continuous* observations of more than 1 day, which enables detailed monitoring of the time evolution of blazars (Table 1). In particular, three "long-look" observations have been conducted, for Mrk 421 (7 days in 1998), Mrk 501 (14 days in 1998), and PKS

TABLE 1

OBSERVATION LOG (CONTINUOUS OBSERVATIONS)

| Source | Satellite | Observing Time (UT) | Exposure[a] (ks) | Figure |
|---|---|---|---|---|
| Mrk 421 ............. | *ASCA* | 1993 May 10 03:22–May 11 03:17 | 43 | 1*a* |
| | *ASCA* | 1994 May 16 10:04–May 17 08:06 | 39 | 1*b* |
| | *ASCA* | 1998 Apr 23 23:08–Apr 30 19:32 | 280 | 1*c* |
| Mrk 501 ............. | *RXTE* | 1998 May 15 12:34–May 29 12:11 | 306 | 1*d* |
| PKS 2155−304...... | *ASCA* | 1993 May 03 20:56–May 04 23:54 | 37 | 1*e* |
| | *ASCA* | 1994 May 19 04:38–May 21 07:56 | 96 | 1*f* |
| | *RXTE* | 1996 May 16 00:40–May 28 15:26 | 161 | 1*g* |

[a] Exposure of GIS for *ASCA* and PCA for *RXTE*.

TABLE 2

OBSERVATION LOG (SHORT OBSERVATIONS)

| Source | Satellite | Observing Time (UT) | Exposure[a] (ks) | Figure |
|---|---|---|---|---|
| Mrk 421 ............. | *ASCA* | 1995 Apr 25 19:16–May 08 13:27 | 91 | 2*A* |
| | *ASCA* | 1997 Apr 29 01:45–May 06 08:32 | 70 | 2*B* |
| Mrk 501 ............. | *RXTE* | 1997 Apr 03 04:27–Apr 16 10:51 | 36 | 2*C* |
| | *RXTE* | 1997 May 02 04:19–May 15 06:49 | 51 | 2*D* |
| | *RXTE* | 1997 Jul 11 23:23–Jul 16 04:55 | 38 | 2*E* |
| | *RXTE* | 1998 Feb 25 17:29–Oct 02 23:06 | 262 | 2*F* |
| PKS 2155−304...... | *RXTE* | 1996 Nov 14 07:39–Nov 24 13:12 | 74 | 2*G* |
| | *RXTE* | 1998 Jan 09 03:07–Jan 13 14:46 | 11 | 2*H* |

[a] Exposure of GIS for *ASCA* and PCA for *RXTE*.

2155−304 (12 days in 1996). For this group, the observing efficiency, which is defined as the ratio of net exposure to the observing time, is about 0.5 for the *ASCA* observation. Interruptions are due to Earth occultation, passages through the South Atlantic Anomaly, etc. For the two *RXTE* observations, the observing efficiency was less: 0.3 for the 14 day monitoring of Mrk 501 and 0.2 for the 12 day monitoring of PKS 2155−304. We use the data from these continuous observations in both the PSD (§ 2.3) and the SF analyses (§ 2.4).

The second group is the *short* observations of a few kiloseconds each, which are spaced typically ≥1 day apart, so that the source can be monitored over as long a time range as possible (Table 2). For these observations, the observing efficiency is less than 0.1 and/or there are large gaps during the observation. These interrupted observations are not suitable for the PSD studies described in § 2.3 but are still useful for investigating the long-term variability based on the SF analysis (§ 2.4).

### 2.2. *Data Reduction*

All the *ASCA* observations listed in Tables 1 and 2 were performed in a normal PH mode for the Gas Imaging Spectrometer (GIS; Ohashi et al. 1996). A normal 4-CCD mode was used for the Solid-State Imaging Spectrometer (SIS; Burke et al. 1991; Yamashita et al. 1997) for 1993 observations, while a normal 1-CCD mode was used for the observations after 1994. Standard screening procedures were applied to the data, and the source counts are extracted from a circular region centered on a target with a radius of 6′ for the GIS and 3′ for the SIS. The count rates of both GIS detectors (GIS 2/3) and SIS detectors (SIS 0/1) are separately summed. Since the count rate of the background (∼ 0.01 counts $s^{-1}$) and its fluctuation are negligible compared with the source count rates (≥1 counts $s^{-1}$), background subtraction was not performed.

For the PKS 2155−304 observation in 1993, we only analyzed the GIS data because the source was so bright that the SIS detector was strongly saturated in 4-CCD mode. Similarly, for the Mrk 421 observation in 1998, when the source was in an historically high state (Takahashi et al. 2000), both the GIS and SIS were saturated during the observation. For this observation, we estimate the GIS count rate from the relation between the GIS count rate and the "hit count" of the lower discriminator (Makishima et al. 1996). The effects caused by saturation of the SIS detectors were corrected by extracting the source counts from a narrower circular region than usual: a radius of 1′ for SIS0 and 2′.6 for SIS1, respectively.

For the *RXTE* observations, source counts from the Proportional Counter Array (PCA; Jahoda et al. 1996) were extracted from three Proportional Counter Units (PCU 0/1/2), which had much larger and less interrupted exposures than those for PCU3 and PCU4. We used only signals from the top layer (X1L and X1R), in order to obtain the best signal-to-noise ratio. Standard screening procedures were performed on the data. Backgrounds were estimated using "pcabackest" (Version 2.1b) for the PCA data. Although there are two other instruments on board *RXTE*, the High Energy X-Ray Timing Experiment (HEXTE) and All-Sky Monitor (ASM), we do not use data from these instruments for two reasons: First, calibration problems make the analysis results quite uncertain for both HEXTE and ASM. Second, the typical exposure for *RXTE* observations was too short to yield statistically meaningful hard X-ray data above 20 keV for HEXTE.

In order to obtain the maximum photon statistics and the best signal-to-noise ratio, we selected the energy range 0.7–10 keV for the *ASCA* GIS, 0.5–10 keV for the *ASCA* SIS, and 2.5–20 keV for the *RXTE* PCA. The light curves for the continuous *ASCA* (GIS)/*RXTE* (PCA) observations (Table 1) are shown in Figures 1*a*–1*g*. We plot the GIS data rather than the SIS data to compare the source count rate, because the GIS has a wider field of view than the SIS and is less affected by the attitude of the satellite and position of the source on the detector. The binning time is 256 s for *ASCA* (GIS) data and 5760 s for the *RXTE* (PCA) observations. Note that 5760 s is the orbital period of both *ASCA* and *RXTE* satellites. Expanded plots of the *RXTE* (PCA) light curves are given in small panels in Figures 1*d* and 1*g*, with a binning time of 256 s. Variability is detected in all of the observations. In particular, for the long-look monitoring of Mrk 421 (1998; Fig. 1*c*), Mrk 501 (1998; Fig. 1*d*), and PKS 2155−304 (1996; Fig. 1*g*), successive flares are clearly seen.

Figure 2 shows the long-term variation of fluxes, with both continuous and short *ASCA* and *RXTE* observations plotted. *ASCA* observations of Mrk 421 spanned more than 5 yr (from 1993 to 1998) and show that the source exhibits variability by more than an order of magnitude. Blowups of the light curves taken in 1995 and 1997 are given in the lower panels (Figs. 2*A* and 2*B*). For Mrk 501 and PKS 2155−304, we plot the *RXTE* data because the observations were conducted much more frequently than the *ASCA* observations. The *RXTE* observations spanned more than 3 yr, and significant flux changes are clearly detected. Blowups of light curves for short observations are given in Figures 2*C*–2*H*.

### 2.3. *Power Spectrum Density*

Power spectrum density analysis is the most common technique used to characterize the variability of the system. The high-quality data obtained with *ASCA* and *RXTE* enable us to determine the PSD over a wider frequency range than attempted previously. An important issue is the data gaps, which are unavoidable for low-orbit X-ray satellites (see Fig. 1). Since the orbital period of *ASCA* and *RXTE* is 5760 s, Earth occultation makes periodic gaps every 5760 s, even for the continuous *ASCA* observations (Table 1). Similarly, the long-look *RXTE* observations of Mrk 501 and PKS 2155−304 (Figs. 1*d* and 1*g*) have artificial gaps, since the observations are spaced typically three or four orbits (17,280 or 23,040 s) apart. To reduce the effects caused by such windowing, we introduce a technique for calculating the PSD of unevenly sampled light curves.

Following Hayashida et al. (1998), the NPSD (*normalized* power spectrum density) at frequency $f$ is defined as

$$P(f) = \frac{[a^2(f) + b^2(f) - \sigma^2_{\rm stat}/n]T}{F^2_{\rm av}} ,$$

$$a(f) = \frac{1}{n}\sum_{j=0}^{n-1} F_j \cos(2\pi f t_j) ,$$

$$b(f) = \frac{1}{n}\sum_{j=0}^{n-1} F_j \sin(2\pi f t_j) , \qquad (1)$$

where $F_j$ is the source count rate at time $t_j$ ($0 \le j \le n-1$), $T$ is the data length of the time series, and $F_{\rm av}$ is the mean

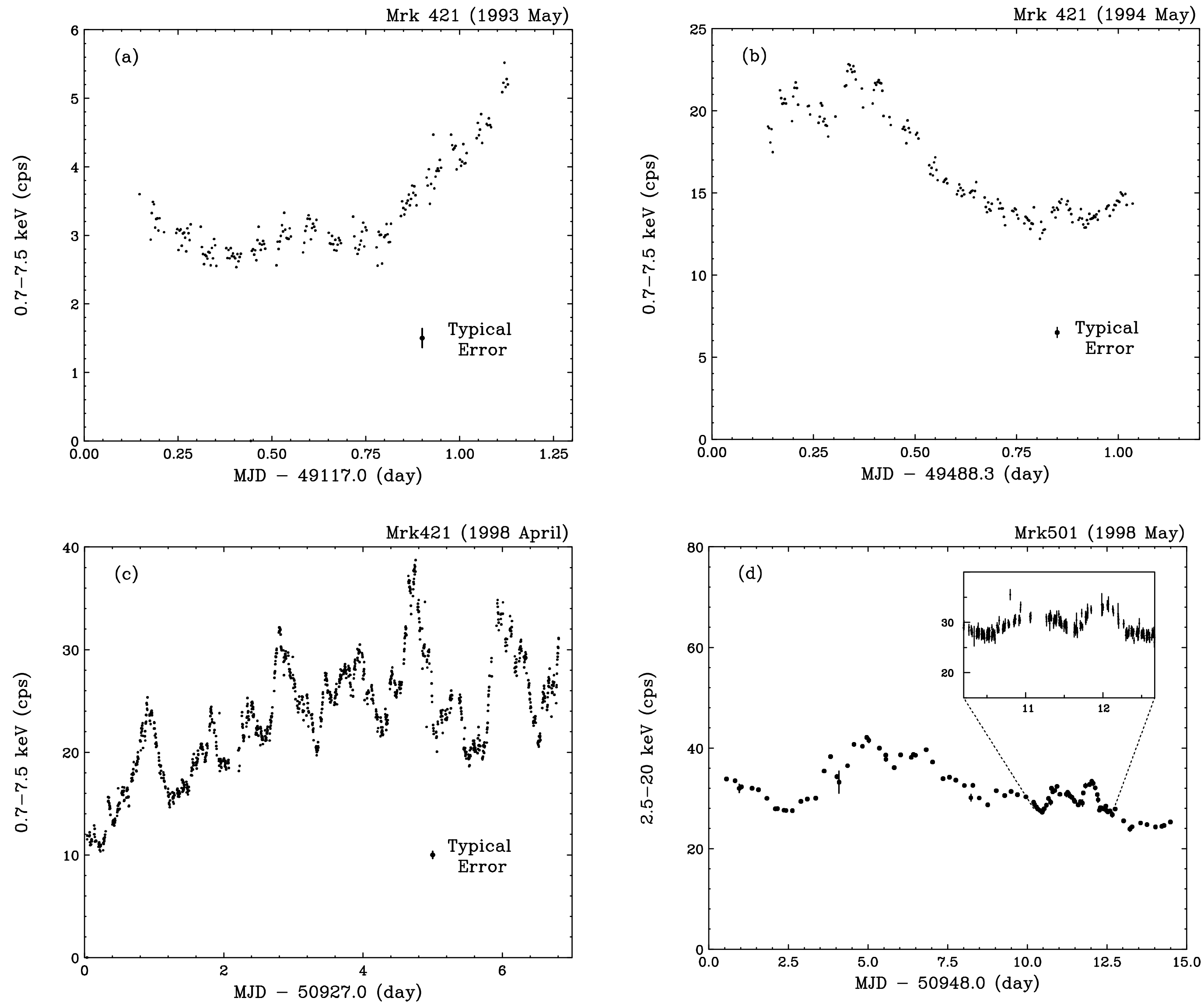


FIG. 1.—X-ray flux variations of TeV blazars in different observations: (*a*) Mrk 421 (1993 May 10–11; *ASCA*), (*b*) Mrk 421 (1994 May 16–17; *ASCA*), (*c*) Mrk 421 (1998 April 23–30; *ASCA*), (*d*) Mrk 501 (1998 May 15–29; *RXTE*), (*e*) PKS 2155 − 304 (1993 May 3–4; *ASCA*), (*f*) PKS 2155 − 304 (1994 May 19–21; *ASCA*), and (*g*) PKS 2155 − 304 (1996 May 16–28; *RXTE*). Observation logs are given in Table 1. For the *ASCA* data, the energy range is 0.7–10 keV, the count rates from both GIS detectors are summed, and the data are binned in 256 s intervals. For the *RXTE* data, the energy range is 2.5–20 keV, the count rates from the three PCUs are summed, and the data are binned in 5760 s intervals.

value of the source counting rate. The power due to the photon-counting statistics is given by $\sigma_{\rm stat}^2$. With our definition, integration of power over the positive frequencies is equal to half of the light curve excess variance (e.g., Nandra et al. 1997).

To calculate the NPSD of our data sets, we made light curves of two different bin sizes for the *ASCA* data (256 and 5760 s) and three different bin sizes for the *RXTE* data (256, 5760, and 23,040 s). We then divided each light curve into "segments," which are defined as the continuous part of the light curve. If the light curve contains a time gap larger than twice the data bin size, we cut the light curve into two segments before/after the gap. We then calculate the power at frequencies $f = k/T$ $(1 \leq k \leq n/2)$ for each segment and take the average.

In this manner, the light curve binned at 256 s is divided into different segments every 5760 s, corresponding to the gap due to orbital period. On the other hand, the light curve binned at 5760 (or 23,040) s is smoothly connected up to the total observation length $T$, if further artificial gaps are not involved. This technique produces a large blank in the NPSD at around $2 \times 10^{-4}$ Hz (the inverse of the orbital period), but the effects caused by the sampling window are minimized. The validity of the NPSD value at other frequencies is discussed in detail in Hayashida et al. (1998). In the following, we calculate the NPSD using the data from the continuous observations in Table 1.

Figures 3*a*–3*g* show the NPSD calculated with this procedure. The upper frequency limit is the Nyquist frequency ($2 \times 10^{-3}$ Hz for 256 s bins), and the lower frequency is about half the inverse of the longest continuous segments. These NPSDs are binned in logarithmic intervals of 0.2 (i.e., factors of 1.6) to reduce the noise. The error bars represent the standard deviation of the average power in each rebinned frequency interval. The expected noise power due to counting statistics, $\sigma_{\rm stat}^2\, T/nF_{\rm av}^2$ (see eq. [1]), are shown in

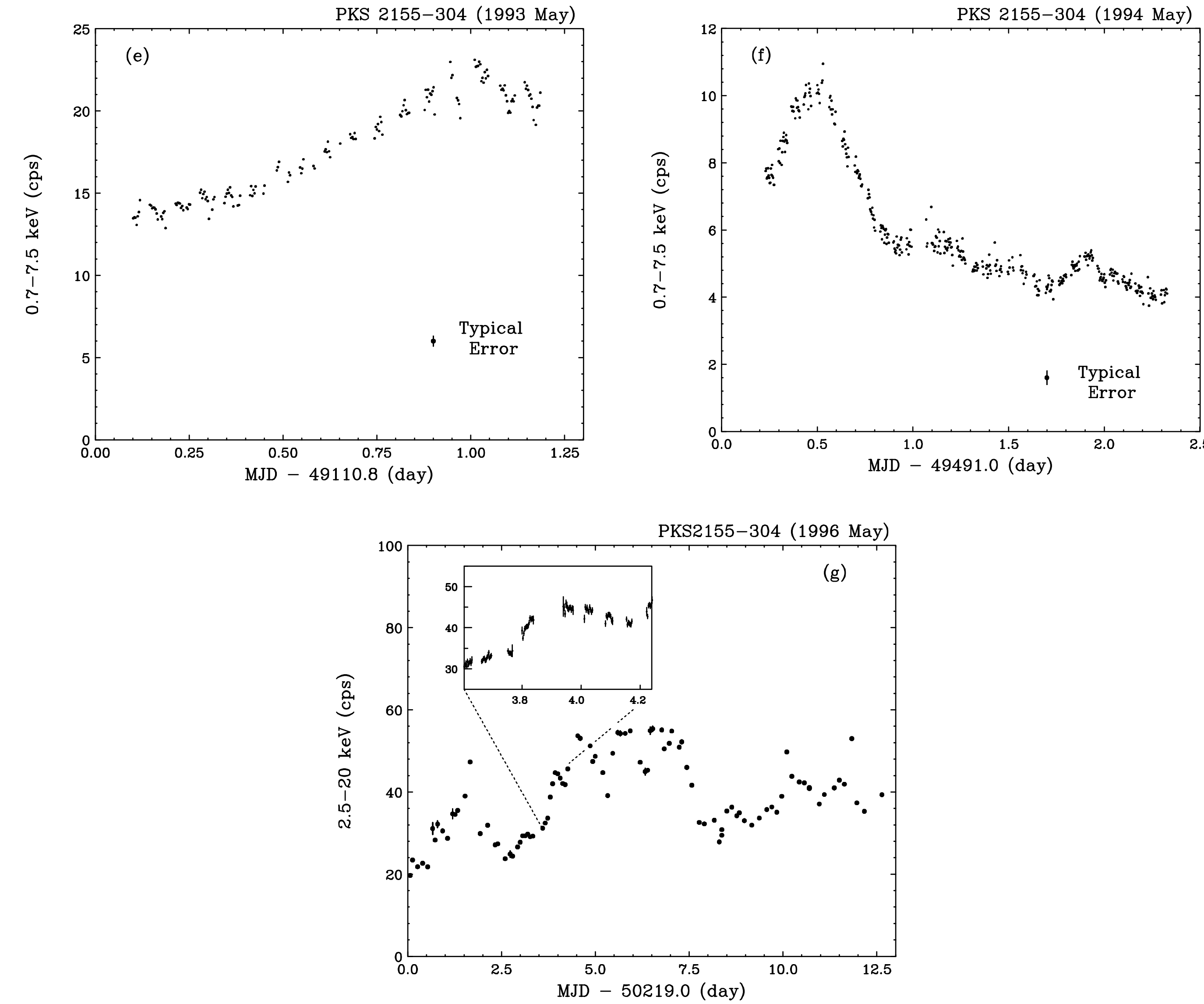


FIG. 1.—*Continued*

each panel as a dashed line. For the *ASCA* data, we calculate the NPSD using both the GIS and the SIS data, while the PCA data were used for the *RXTE* light curves (see Fig. 1).

One finds that the NPSDs follow a power law that decreases with increasing frequency in the high-frequency range. For the long-look observations of Mrk 421 (1998; Fig. 3*c*), Mrk 501 (1998; Fig. 3*d*), and PKS 2155−304 (1996; Fig. 3*g*), signs of a rollover can be seen at the low-frequency end ($f \sim 10^{-5}$ Hz). Since all the NPSDs have very steep power-law slopes, only little power exists above $10^{-3}$ Hz. This is very different from the PSDs of Seyfert galaxies, for which powers are well above the counting noise up to $10^{-2}$ Hz (e.g., Hayashida et al. 1998; Nowak & Chiang 2000). Note that this is *not* due to low counting statistics, because the TeV sources discussed here are much brighter in X-rays than most Seyfert galaxies.

To quantify the slope of the NPSD, we first fit a *single* power law to each NPSD in the frequency range $f \leq 10^{-3}$ Hz. We do not use the data above $10^{-3}$ Hz because they tend to be noisy and often consistent with zero power. The results are summarized in Table 3. A single–power-law function turned out to be a good representation of all observations except for those of Mrk 421 (1998; Fig. 3*c*), Mrk 501 (1998; Fig. 3*d*), and PKS 2155−304 (1996; Fig. 3*g*). The best-fit power-law slopes ($\alpha$ of $f^{-\alpha}$) range from ∼2 to 3, indicating a strong red-noise behavior. For the three long-

TABLE 3

FITTING RESULTS OF THE NPSD WITH A SINGLE POWER LAW

| Source | Observation[a] | $\alpha$[b] | $\chi^2$ (dof) |
|---|---|---|---|
| Mrk 421 ............. | *ASCA* 1993 | 2.56 ± 0.09 | 18.2 (11) |
| | *ASCA* 1994 | 2.14 ± 0.24 | 15.2 (10) |
| | *ASCA* 1998 | 2.03 ± 0.03 | 39.7 (23)[c] |
| Mrk 501 ............. | *RXTE* 1998 | 1.88 ± 0.07 | 32.2 (11)[c] |
| PKS 2155−304...... | *ASCA* 1993 | 2.14 ± 0.22 | 3.9 (4) |
| | *ASCA* 1994 | 3.10 ± 0.20 | 17.2 (15) |
| | *RXTE* 1996 | 1.90 ± 0.03 | 22.6 (11)[c] |

[a] GIS data (0.7–10 keV) and SIS data (0.5–10 keV) were used for *ASCA* observations, and PCA data (2.5–20 keV) were used for *RXTE* observations.

[b] The best-fit power-law index of NPSDs ($\alpha$ of $f^{-\alpha}$).

[c] Goodness of the fit is bad, with $P(\chi^2) < 0.02$.

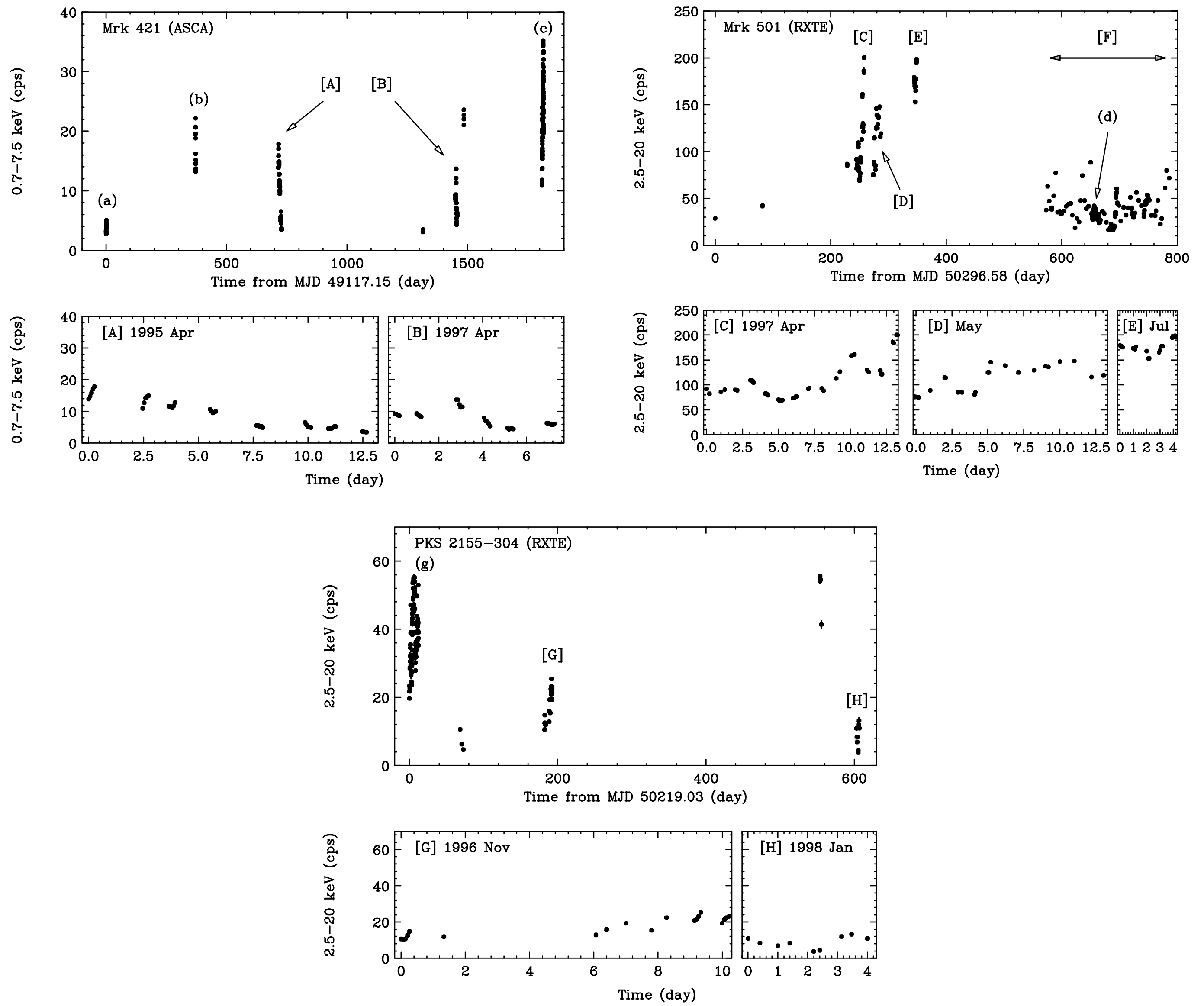


FIG. 2.—Long-term flux variation of three TeV sources: Mrk 421 (1993 May 10 to 1998 April 30 with *ASCA*), Mrk 501 (1996 August 1 to 1998 October 2 with *RXTE*), and PKS 2155−304 (1996 May 16 to 1998 January 13 with *RXTE*). Energy ranges are the same, and count rates were determined the same way, as for Fig. 1. Observation logs for parentheses are given in Table 1, while logs for square brackets are given in Table 2. Small lower panels are expanded plots of the light curves.

look observations, this model did not represent the NPSD adequately; the power law fitting the data below $10^{-5}$ Hz was too flat for the data above $10^{-5}$ Hz. For these observations, the $\chi^2$ was 39.7 (23 degrees of freedom [dof]) for Mrk 421, 32.2 (11 dof) for Mrk 501, and 22.6 (11 dof) for PKS 2155−304. A single–power-law model is thus rejected with a higher than 98% confidence level for these long-look observations.

A better fit was obtained using a *broken* power-law model, where the spectrum is harder below the break. The fitting function used was $P(f) \propto f^{-\alpha_L}$ for $f \leq f_{\rm br}$ and $P(f) \propto f^{-\alpha}$ for $f > f_{\rm br}$. With this relatively simple model, the exact shape of the turnover is not well constrained, and the low-frequency behavior is undetermined. We thus fixed $\alpha$ at the best-fit value determined from a power-law fit in the high-frequency range of $10^{-5}$ to $10^{-3}$ Hz and kept $\alpha_L$ and $f_{\rm br}$ as free parameters. The fitting results are given in Table 4. The goodness of the fit was significantly improved: 21.1 (22 dof), 18.6 (10 dof), and 3.9 (10 dof) for Mrk 421, Mrk 501, and PKS 2155−304, respectively. For these three sources, the break frequency ranges from 1.0 to 3.0 × $10^{-5}$ Hz, roughly consistent with the apparent timescale of successive flares seen in Figure 1. Below the break, the slope of the NPSD ($\alpha_L$) is relatively flat, ranging from 0.9 to 1.5.

Finally, we comment on the effects caused by sampling windows. As mentioned above, our PSD technique is less affected by the sampling windows, because only the continuous parts of the light curve are used for the calculation. In fact, this seems to have negligible effects for the *ASCA* data, because the interruptions are almost even and the observing efficiency is high (∼0.5). However, for the *RXTE* data, sampling effects may be significant because the observations are conducted less frequently and the observing efficiency is low (0.2 or 0.3). The most rigorous estimate of this effect would be obtained by simulating the light curves characterized with a certain PSD, filtered by the same window as the

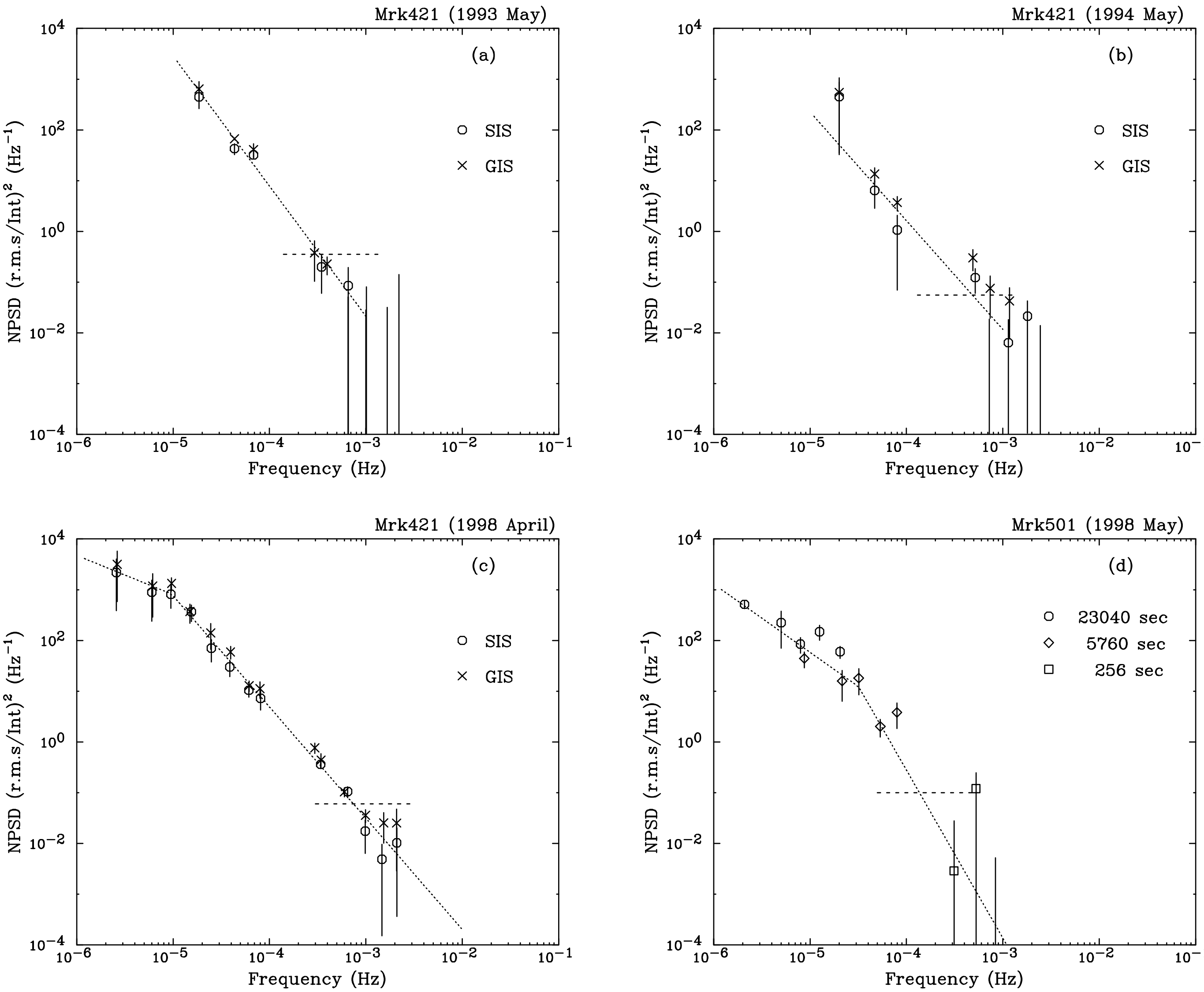


FIG. 3.—Normalized PSD calculated from the light curves in Fig. 1 (for the *ASCA* data, both GIS and SIS data are used for the calculation): (*a*) Mrk 421 (1993 May 10–11; *ASCA*), (*b*) Mrk 421 (1994 May 16–17; *ASCA*), (*c*) Mrk 421 (1998 April 23–30; *ASCA*), (*d*) Mrk 501 (1998 May 15–29; *RXTE*), (*e*) PKS 2155 − 304 (1993 May 3–4; *ASCA*), (*f*) PKS 2155 − 304 (1994 May 19–21; *ASCA*), and (*g*) PKS 2155 − 304 (1996 May 16–28; *RXTE*). Measurement noise, at the level shown by the dashed line in each figure, has been subtracted from each point. The best-fit power-law function or broken power law is given as dotted lines.

actual observation. The resulting PSDs could then be compared with that we assumed. However, such an estimate is only possible when we already know the *true* PSD of the system.

As an alternative approach, we approximate each data gap by an interpolation of actual data, fitted to a linear function. The gaps in the light curve are thus bridged in a smooth way over the total observation length. We note that, even if the data are linearly interpolated across the gaps, Poisson errors associated with these points remain quite uncertain. We therefore calculated the NPSD in the frequency range $f < 2 \times 10^{-4}$ Hz, where counting errors become negligible compared to the power due to intrinsic source variability (see Fig. 3, *dashed lines*). We tested this

TABLE 4

FIT RESULTS OF THE NPSD WITH A BROKEN POWER LAW

| Source Name | Observation | $\alpha_L$[b] | $\alpha$[c] | $f_{br}$[d] | $\chi^2$ (dof) |
|---|---|---|---|---|---|
| Mrk 421 .............. | *ASCA* 1998 | $0.88 \pm 0.43$ | 2.14 (fixed) | $(9.5 \pm 0.1) \times 10^{-6}$ | 21.1 (22) |
| Mrk 501 .............. | *RXTE* 1998 | $1.37 \pm 0.16$ | 2.92 (fixed) | $(3.0 \pm 0.9) \times 10^{-5}$ | 18.6 (10) |
| PKS 2155−304...... | *RXTE* 1996 | $1.46 \pm 0.10$ | 2.23 (fixed) | $(1.2 \pm 0.4) \times 10^{-5}$ | 3.9 (10) |

[a] GIS data (0.7–10 keV) and SIS data (0.5–10 keV) were used for *ASCA* observations, and PCA data (2.5–20 keV) were used for *RXTE* observations.

[b] The best-fit broken power-law index of NPSDs below the break frequency $f < f_{br}$.

[c] The best-fit power-law index of NPSDs in the region of $10^{-5}$ Hz $< f < 10^{-3}$ Hz.

[d] The best-fit break frequency $f_{br}$.

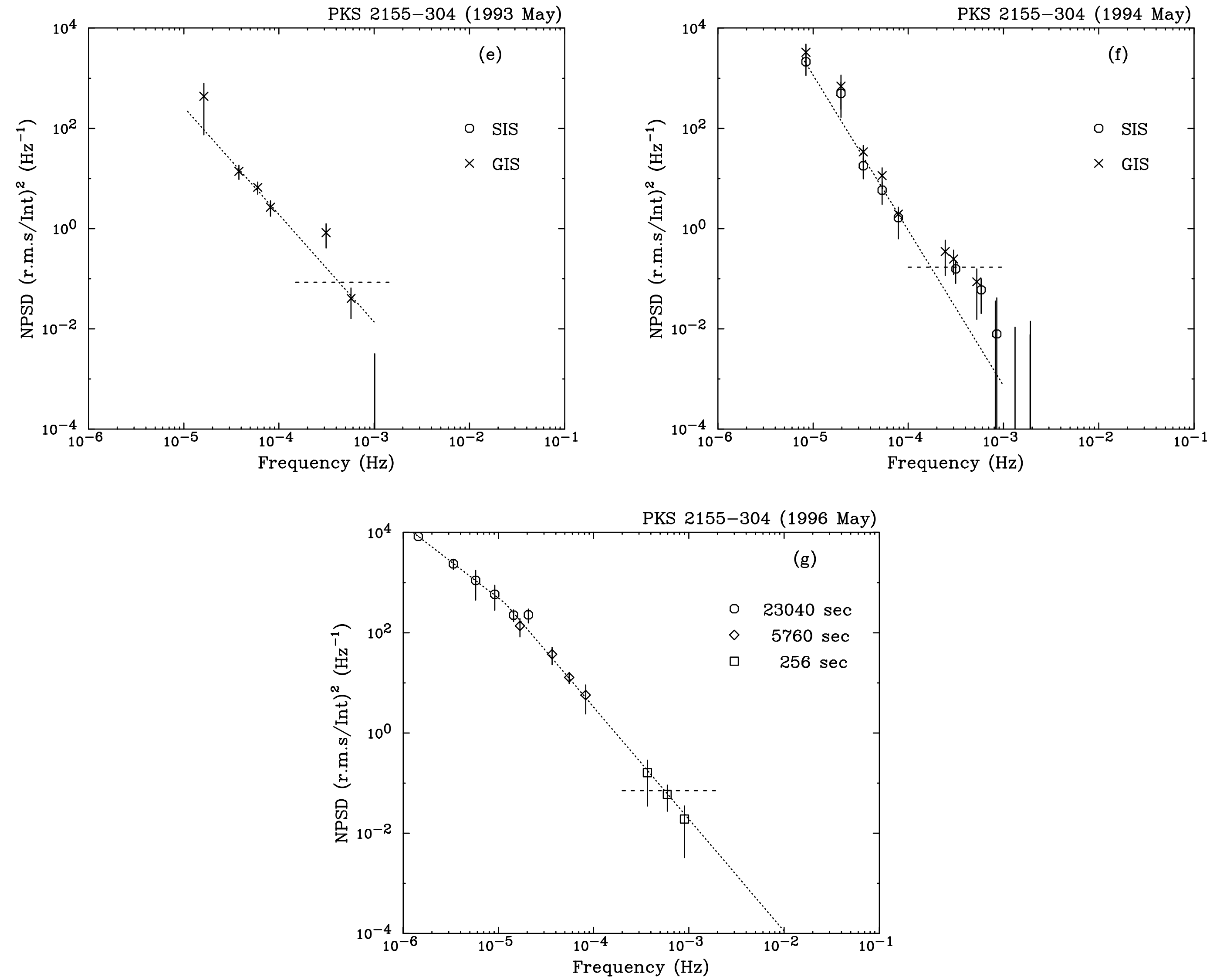


FIG. 3.—*Continued*

interpolation method for the data of the three long-look observations.

We found that the NPSDs calculated from this interpolation method are entirely consistent with those given in Table 4 for both Mrk 421 and PKS 2155−304. For Mrk 501, $\alpha$ and $\alpha_L$ are consistent, but $f_{\rm br}$ is estimated to be $(1.3 \pm 0.4) \times 10^{-5}$ Hz, which is slightly smaller than the value in Table 4 [viz., $(3.0 \pm 0.9) \times 10^{-5}$ Hz]. Such a difference, however, could be due to poor statistics of the NPSD plots (Fig. 3*d*) rather than the sampling effects discussed here. In fact, we have to determine $f_{\rm br}$ only from several data points around the turnover. Moreover, although we have fitted the NPSD with $\alpha$ fixed to the best-fit value of 2.92 (see Table 4), a wider range of $f_{\rm br}$ would be acceptable when all parameters are allowed to vary.

Also note that such interpolations might introduce large systematics in the resulting PSD when the observing efficiency is low. In fact, interpolations of the observed data to fill the gaps would produce the *smoothest* possible solution, because it assumes the least variations across the observational data. This might affect the resulting PSD slopes ($\alpha$ and $\alpha_L$) as well as the break frequency ($f_{\rm br}$), especially for the *RXTE* observations. The exact position of a break is thus unclear, but conservatively, we can give a frequency $f_{\rm br} \simeq 10^{-5}$ Hz with an uncertainty factor of a few or larger. In the next section, we thus consider a wide range for the rollovers ($f_{\rm br}$), using the more powerful structure function technique.

### 2.4. *Structure Function*

In this section we examine the use of a numerical technique called the structure function. The SF can potentially provide information on the nature of the physical process causing any observed variability. While in theory the SF is completely equivalent to traditional Fourier analysis methods (e.g., the PSD; § 2.3), it has several significant advantages: First, it is much easier to calculate. Second, the SF is less affected by gaps in the light curves (e.g., Hughes, Aller, & Aller 1992). The definitions of SFs and their properties are given by Simonetti, Cordes, & Heeschen (1985). The first-order SF is defined as

$$\mathrm{SF}(\tau) = \frac{1}{N} \sum \left[a(t) - a(t+\tau)\right]^2 , \qquad (2)$$

where $a(t)$ is a point of the time series (light curves) $\{a\}$ and the summation is made over all pairs separated in time by $\tau$.

The term $N$ is the number of such pairs. Note that the SF is free from the constant offset in the time series, whereas techniques such as the autocorrelation function (ACF) and the PSD are not.

The SF is closely related to the power spectrum density distribution. If the structure function has a power-law form, $\mathrm{SF}(\tau) \propto \tau^{\beta}$ ($\beta > 0$), then the power spectrum has the distribution $P(f) \propto f^{-\alpha}$, where $f$ is frequency and $\alpha \simeq \beta + 1$. We note that this approximation is invalid when $\alpha$ is smaller than 1. In fact, both the SF and the NPSD should have zero slope for white noise, because it has a zero correlation timescale. However, the relation holds within an error of $\Delta\alpha \simeq 0.2$ when $\alpha$ is larger than $\sim 1.5$ (e.g., Paltani et al. 1997; Cagnoni, Papadakis, & Fruscione 2001; Iyomoto & Makishima 2001). Therefore, the SF gives a crude but convenient estimate of the corresponding PSD distribution, which characterizes the variability.

In general, the SF gradually changes its slope ($\beta$) with time interval $\tau$. On the shortest timescale, variability can be well approximated by a linear function of time: $a(t) \propto t$. In this time domain, the resulting SF is $\propto \tau^2$, which is the steepest portion in the SF curve (see eq. [2]). For longer timescales, the slope of the SF becomes flatter ($\beta < 2$), reflecting the physical process operating in the system. When $\tau$ exceeds the longest time variability of the system, the SF further flattens, with $\beta \sim 0$, which is the flattest portion in the SF curve (white noise). At this end, the amplitude of the SF is equal to twice the variance of the fluctuation.

In Figure 4, the SFs are plotted for the light curves presented in Figure 1. *ASCA* (GIS) and *RXTE* (PCA) light curves binned in 1024 s intervals are used for the calculation. The resulting SFs are normalized by the square of the mean fluxes and are binned at logarithmically equal intervals. The measurement noise (Poisson errors associated with flux uncertainty) is subtracted as twice the square of Poisson errors on the fluxes: $2\langle \delta a^2 \rangle$. The noise level is shown as a dashed line in the figures. All the SFs are charac-

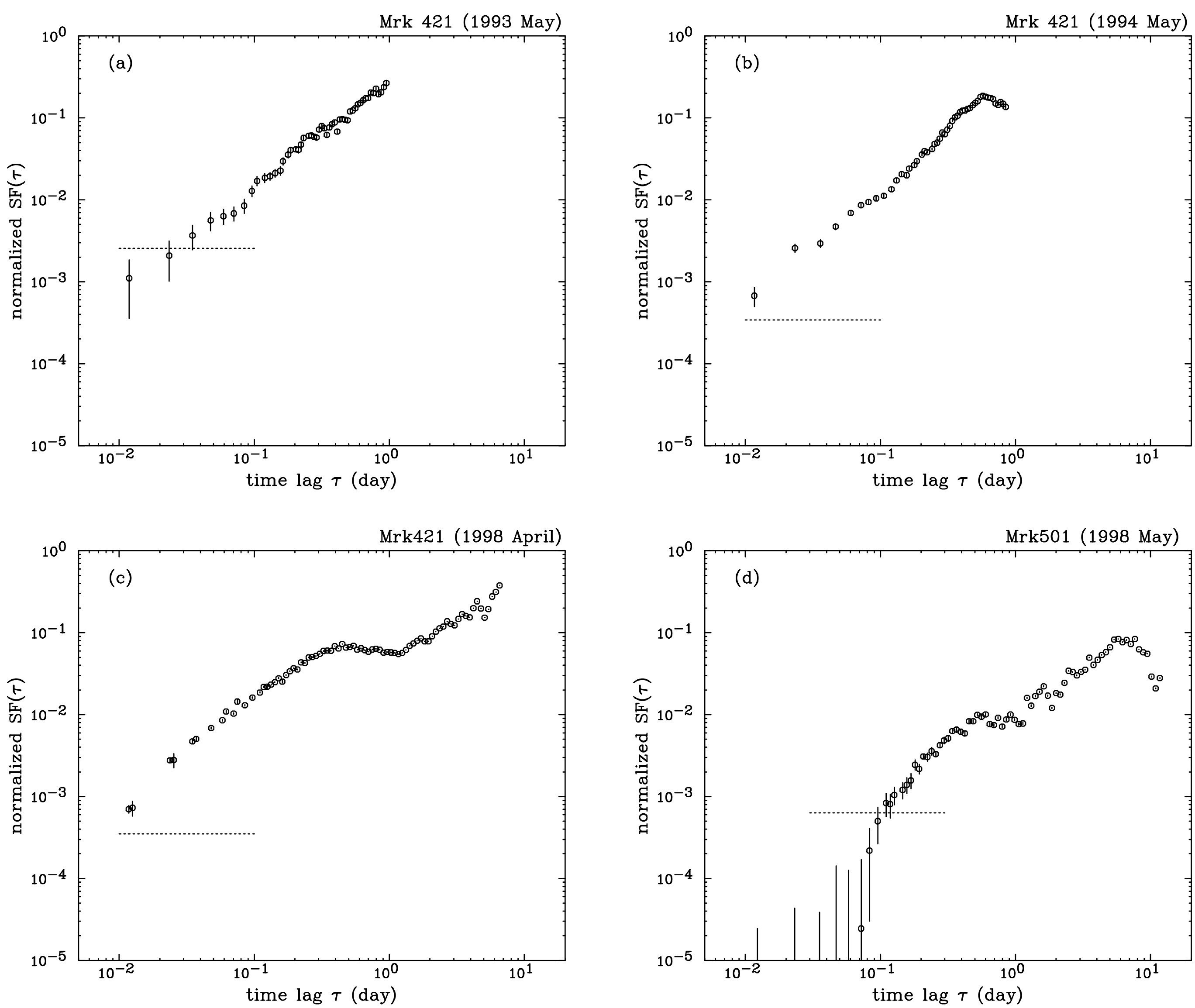


FIG. 4.—Structure functions calculated from the light curves in Fig. 1 (each SF is normalized by the square of the mean fluxes): (*a*) Mrk 421 (1993 May 10–11; *ASCA*), (*b*) Mrk 421 (1994 May 16–17; *ASCA*), (*c*) Mrk 421 (1998 April 23–30; *ASCA*), (*d*) Mrk 501 (1998 May 15–29; *RXTE*), (*e*) PKS 2155 − 304 (1993 May 3–4; *ASCA*), (*f*) PKS 2155 − 304 (1994 May 19–21; *ASCA*), and (*g*) PKS 2155 − 304 (1996 May 16–28; *RXTE*). Measurement noise, at the level shown by the dashed line in each figure, has been subtracted from each point.

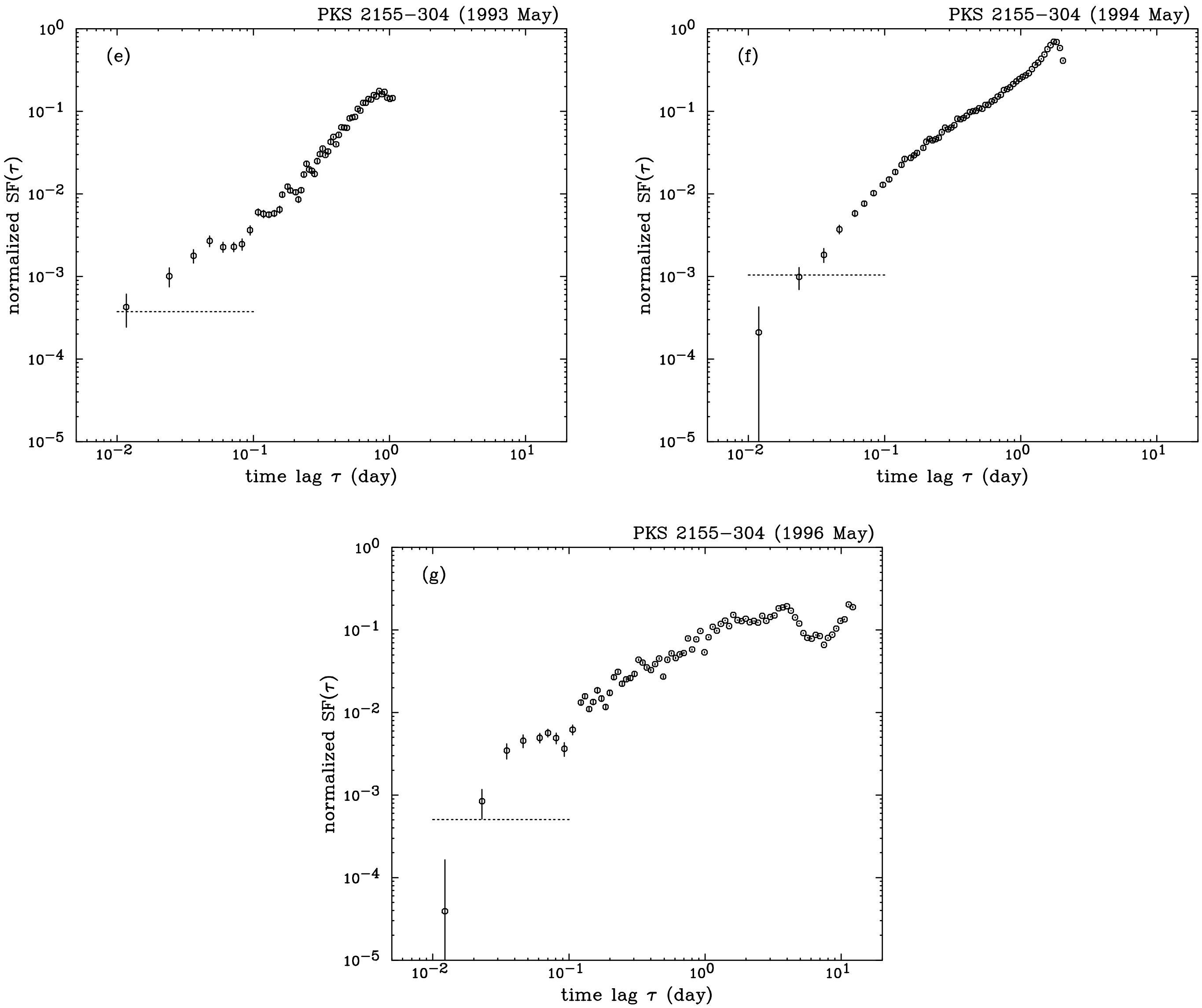


FIG. 4.—*Continued*

terized with a steep increase ($\beta > 1$) in the time region of $10^{-2} < \tau/\mathrm{day} < 1$, roughly consistent with the corresponding NPSDs given in Figure 3 [$P(f) \propto f^{-2\sim-3}$].

The SFs of the long-look observations show a variety of features. For example, the SF of Mrk 421 (Fig. 4*c*) shows a very complex SF that cannot even be described as a simple power law, as it flattens around 0.5 days, then steepens again around 2 days. A similar rollover can be seen for Mrk 501 and PKS 2155−304 around 1 day (Figs. 4*d* and 4*g*). Importantly, these turnovers reflect the typical timescale of repeated flares, corresponding to the break in the NPSDs described in § 2.3. The complicated features (rapid rise and decay) at large $\tau$ may not be real and may result from the insufficiently long sampling of data. The number of pairs in equation (1) decreases with increasing $\tau$, and hence the resulting SF becomes uncertain as $\tau$ approaches $T$, where $T$ is the length of the time series. The statistical significance of these features can be tested using the Monte Carlo simulation described below.

We next calculate the structure functions using the total light curves given in Figure 2. Using 5 yr of *ASCA* data and 3 yr of *RXTE* data, we can investigate the variability in the widest time domain over more than 5 orders: $10^{-2} \leq \tau/\mathrm{day} \leq 10^3$. The results are respectively given for Mrk 421, Mrk 501, and PKS 2155−304 in Figure 5. Filled circles are observational data, normalized by the square of the mean fluxes, and are binned at logarithmically equal intervals. All the SFs show a rapid increase up to $\tau/\mathrm{day} \simeq 1$, then gradually flatten to the observed longest timescale of $\tau/\mathrm{day} \geq 1000$. Fluctuations at large $\tau$ ($\tau/\mathrm{day} \geq 10$) are due to the extremely sparse sampling of data. In fact, even for the case of Mrk 501 (the most frequently sampled data), the total observation time is 700 ks, which is only 1% of the total span of 3 yr. Although we cannot apply the usual PSD technique to such undersampled data, it appears the SF still can be a viable estimator.

In order to demonstrate the uncertainties caused by such sparse sampling and to firmly establish the reality of the rollover, we simulated the long-term light curves (Fig. 2) following the *forward method* described in Iyomoto (1999). We first assume a certain PSD that describes the characteristic variability of the system. Using a Monte Carlo technique, we generate a set of random numbers uniformly distributed between 0 and $2\pi$ and use them as the random phases of the Fourier components. A fake light curve is then generated by a Fourier transformation, with the constraint

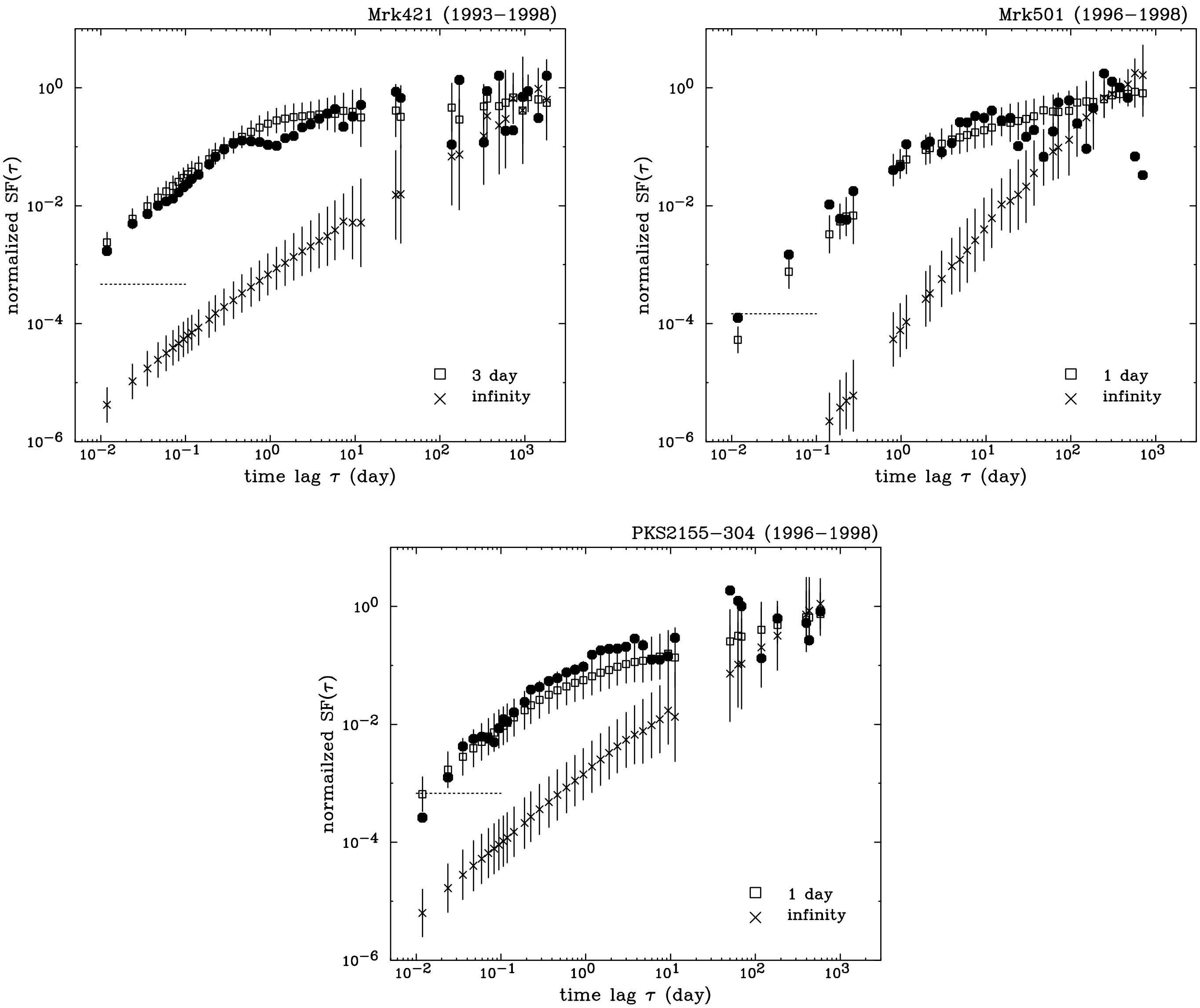


FIG. 5.—Structure functions of Mrk 421, Mrk 501, and PKS 2155−304, based on long-term light curves presented in Fig. 2. Filled circles represent the observational data, crosses represent simulated SFs assuming a single–power-law NPSD ($1/f_{\rm br} = \infty$), and open squares represent simulated SFs assuming a broken power-law NPSD ($1/f_{\rm br} = 1$ or 3 days). Each SF is normalized by the square of the mean fluxes. Measurement noise, at the level shown by the dashed line in each figure, has been subtracted from each point.

that the power in each frequency bin decreases as specified by the PSD. We simply choose a deterministic amplitude for each frequency and randomize only the phases, a common approach (e.g., Done et al. 1992). It may be most rigorous to also assume "random amplitudes" distributed within 1 $\sigma$ of the input PSD (Timmer & König 1995), but simulations based on their algorithm remain as a future work.

The resulting light curve is filtered by the same sampling window as the actual observation and is normalized to have the same rms as the actual data. We repeat this process using different sets of random numbers and generate 1000 light curves for the assumed PSD. Finally, the SFs are calculated for the individual light curves. We found that simulated SFs generally show the same kinds of bumps and wiggles as the real data and sometimes show a rollover even if none was simulated. Several examples of simulated SFs are shown in Figure 6. Such "structures" often appeared at large $\tau$, probably because of the finite length of the light curve. We perform the same statistical test to these simulated data for quantitative comparison with the actual SF.

We first applied this technique assuming a PSD of the form $P(f) \propto f^{-\alpha}$, where $\alpha$ is determined from the best-fit NPSD parameters given in Table 4. In order to reproduce the long-term light curves of Mrk 421, Mrk 501, and PKS 2155−304, we take $\alpha = 2.1$, 2.9, and 2.2, respectively. Based on a set of 1000 fake light curves, we computed the expected mean value, $\langle SF_{\rm sim}(\tau) \rangle$, and variance, $\sigma_{SF(\tau)}$, of all the simulated SFs at each $\tau$. The results are superimposed in Figure 5 as crosses. Errors on simulated data points are equal to $\pm\sigma_{SF(\tau)}$. One finds that errors become larger at large $\tau$, meaning that the SF tends to involve fake bumps and wiggles near the longest observed timescale. Also note that we cannot use these errors in the normal $\chi^2$ estimation, since the actual SF is *not* normally distributed. Large deviations between the actual SFs (*filled circles*) and the simulated ones (*crosses*) are apparent, but quantitative comparison with actual data is necessary.

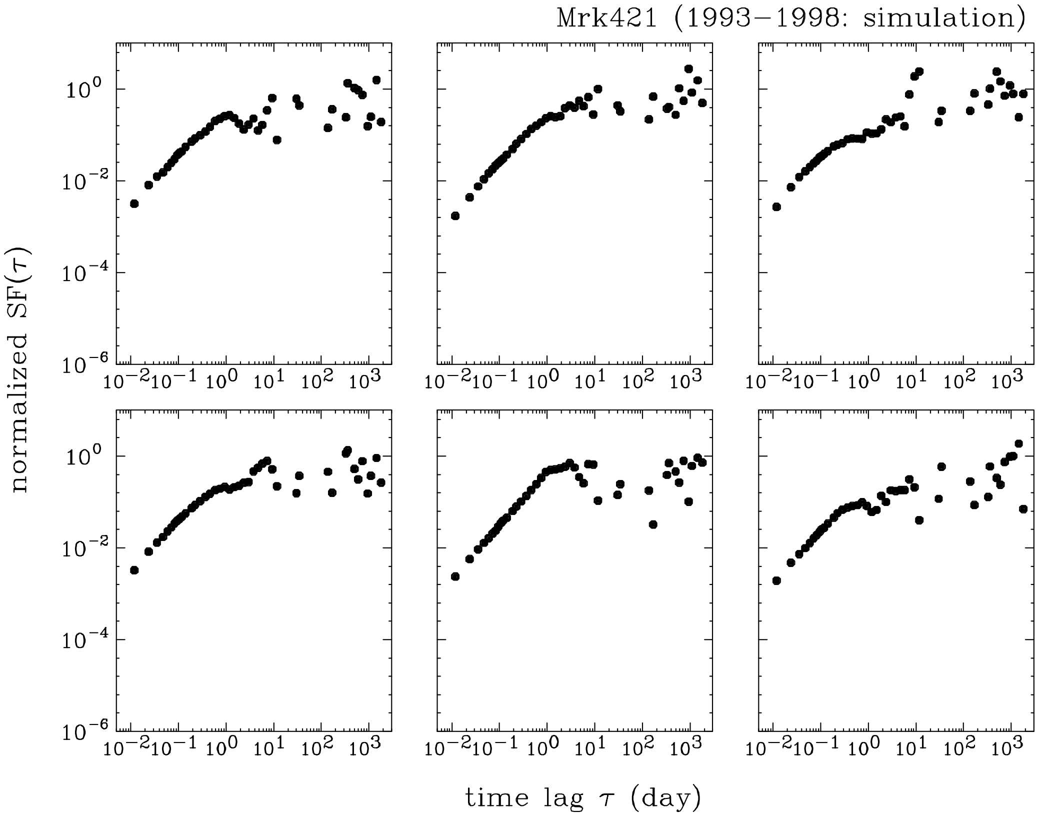


FIG. 6.—Examples of simulated SFs for Mrk 421 data taken in 1993–1998. The corresponding observational results are shown in Fig. 5 (Mrk 421). The PSD is assumed to have a broken power law where the break timescale is 3 days. Full details are given in the text.

To evaluate the statistical significance of the goodness of fit and to test the reality of complicated features in the SF, we then calculate the sum of squared differences, $\chi^2_{\rm sim} = \sum_k \{\log [\langle {\rm SF}_{\rm sim}(\tau_k)\rangle] - \log [{\rm SF}(\tau_k)]\}^2$. Strictly speaking, $\chi^2_{\rm sim}$ defined here is different from the traditional $\chi^2$, but the statistical meaning is the same. For the actual SFs, these values are $\chi^2_{\rm sim} = 1608$, 702, and 521 for Mrk 421, Mrk 501, and PKS 2155−304, respectively. We then generated *another* set of 1000 simulated light curves and hence fake SFs to evaluate the distribution of $\chi^2_{\rm sim}$ values. From this simulation, the probability that the X-ray light curves are the realization of the assumed PSDs is $P(\chi^2) < 10^{-3}$ (0 of 1000 simulated light curves, none of which are a good expression of the data).

We thus introduce a "break," below which the slope of the PSD becomes flatter. Similar to § 2.3, we assume a PSD of the form, $P(f) \propto f^{-\alpha_L}$ for $f < f_{\rm br}$ and $P(f) \propto f^{-\alpha}$ for $f > f_{\rm br}$, where $\alpha$ and $\alpha_L$ were set to the best-fit value given in Table 4, namely, $(\alpha_L, \alpha) = (0.9, 2.1)$ for Mrk 421, (1.4, 2.9) for Mrk 501, and (1.5, 2.2) for PKS 2155−304. Since the exact position of a break is not well constrained, we simulate various cases of $f_{\rm br} = 3.9 \times 10^{-5}$, $1.2 \times 10^{-5}$, and $3.9 \times 10^{-6}$ Hz, which correspond to the break in the SF at $\tau/{\rm day} \simeq 0.3$, 1, and 3, respectively.

As a result, the statistical significance is significantly improved. The results are given in Figure 5 as open squares. For Mrk 421, $\chi^2$ of the actual data is minimized when $f_{\rm br} = 3.9 \times 10^{-6}$ Hz [$\chi^2 = 47$; $P(\chi^2) = 0.59$], but other values for $f_{\rm br}$ are not a good representation of the data. For Mrk 501, both $f_{\rm br} = 1.2 \times 10^{-5}$ and $3.9 \times 10^{-6}$ Hz are acceptable in the meaning that $0.1 < P(\chi^2) < 0.9$ ($\chi^2 = 75$ and 71, respectively). Similarly, the SF of PKS 2155−304 is acceptable for the breaks of $f_{\rm br} = 1.2 \times 10^{-5}$ and $3.9 \times 10^{-6}$ Hz, with $\chi^2 = 21$ and 43 [$P(\chi^2) = 0.74$ and 0.57, respectively]. To obtain an upper limit of the variability timescale, we further tested the case when $f_{\rm br} = (0.3 - 1) \times 10^{-6}$ Hz, which corresponds to the break in the SF at $\tau/{\rm day} \simeq 10$–30, none of which turned out to be acceptable. Thus, although the exact position of the break is still uncertain, the possibility that the X-ray light curves are the realizations of a *single*–power-law PSD can be rejected. We thus conclude that (1) the PSDs of the TeV sources have at least one rollover at $10^{-6}$ Hz $\leq f_{\rm br} \leq 10^{-5}$ Hz ($1 \leq \tau/{\rm day} \leq 10$) and (2) the PSD changes its slope from $\propto f^{-1\sim-2}$ ($f < f_{\rm br}$) to $\propto f^{-2\sim-3}$ ($f > f_{\rm br}$) around the rollover.

We finally refer to the long-term variability of Mrk 501 and its sampling pattern (Fig. 2). As mentioned in § 2.1, Mrk 501 was in a historically high state in 1997, with the result that three of the four observations listed in Table 2 are (more or less) intentionally conducted during this high state. The SF takes existing data points at certain epochs out of an (unknown) *true* variation, implicitly assuming them to be representative of the system. Strictly speaking, the SF analysis will only be valid if the epochs of the observations are randomly chosen regardless of activity of the system. This seems not to be the case with the *RXTE* data of Mrk 501 because observations are *biased* to the high state in 1997 (125 ks of the total 700 ks exposure). To see the effects caused by this sampling pattern, we also performed the SF analysis using only the data taken in 1998. The resulting SF had a very similar shape, but the absolute value of the SF at each $\tau$ tended to be smaller by a factor of $\sim 5$, which means that amplitude of variation is smaller by a factor of $\sim 2$ in 1998 (see Fig. 2). In spite of such difference, the most important part of the result did not change: the PSD of Mrk 501 needs at least one rollover at $10^{-6}$ Hz $\leq f_{\rm br} \leq 10^{-5}$ Hz.

## 3. DISCUSSION

### 3.1. *Comparison with Previous Works*

As seen in § 2, the short-timescale variability of the TeV sources can be described by a steep PSD index up to the characteristic timescale of order or longer than 1 day. This is evidence that only little variability exists on timescales shorter than $t_{\rm var}$, indicating strong red-noise–type behavior. In this section, we compare our results with those given in the literature.

PKS 2155−304 is the only TeV blazar for which PSD studies had previously been made in the X-ray band. Tagliaferri et al. (1991) analyzed *EXOSAT* data (exposure of $\sim 1$ day) and found that the power spectrum follows a power law with an index $-2.5 \pm 0.2$. Hayashida et al. (1998) derived the PSD of PKS 2155−304 from a *Ginga* observation. They reported a PSD index of $-2.83^{+0.35}_{-0.24}$. In the optical, Paltani et al. (1997) studied the variability based on 15 nights' data. They found that the PSD of optical data follows a steep power law of an index $-2.4$ as well. In summary, PSDs in the literature showed featureless red-noise spectra, which are comparable with our results. Very recently, Zhang et al. (1999) analyzed three X-ray light curves obtained with *ASCA* and *BeppoSAX*. They reported a steep PSD index of $-2.2$ for two data sets, but an exception was found during the *BeppoSAX* observation in 1997, which yielded a relatively flat PSD slope of $-1.54 \pm 0.07$.

For Mrk 421 and Mrk 501, no PSD studies have been reported for X-ray variability prior to our work. In the extreme-UV band, Cagnoni et al. (2001) analyzed Mrk 421 data obtained with the *Extreme Ultraviolet Explorer* over a 4 yr period. They reported that the PSD of Mrk 421 is well represented by a slope of $-2.14 \pm 0.28$ with a break at $\sim 3$ days. Similarity of the characteristic timescale and PSD slopes in both the X-ray and EUV bands is very interesting, because it may prove that the emission sites of the X-ray and EUV photons are the same (or very close) in the relativistic jet (see § 3.3). Although high undersampling does not allow us to test whether or not the break frequency is the same in both bands, future studies based on larger samples of data could clarify this point.

Also, it is interesting to note that a break in the SFs and PSDs occurs on the same timescale (of about 20–30 hr) as seen in other blazars in different energy regimes. The frequent occurrence of this preferred timescale in the optical regime (Wagner & Witzel 1995; Heidt & Wagner 1996) is particularly noteworthy, since optical observations are clearly intrinsic and not affected by interstellar scattering. They are almost certainly unaffected by contributions of inverse Compton scattering as well, and the break in the SF occurs at the same timescale as observed here for sources in which the synchrotron component extends well into the X-ray regime. This suggests that the timescale is not due to $\gamma$-$\gamma$ pair absorption or any process that is correlated to the cutoff frequency of the synchrotron branch. The phenomenon of intraday variability (indicating maximum amplitudes for variations on timescales of the order of 1 day; Wagner & Witzel 1995) clearly extends into the X-ray regime as well.

Finally, we briefly comment on the red-noise leak, which might be important to characterize the variability in blazars. In general, the PSD is a biased estimator because of the finite length of real observations. In particular, it is pointed out that large amounts of power could leak through from low to high frequencies when $\alpha$ of $f^{-\alpha}$ is larger than 2 (strong red noise; Deeter & Boynton 1982). For example, Papadakis & Lawrence (1995) studied a simulated time series with a power spectrum that followed $f^{-2.8}$ and flattened below a certain frequency. They found that when the data length is shorter than 10 times the break timescale (which is very similar to our situation), the resulting PSD is biased. A considerable amount of power has been transferred from low to high frequencies, and the resulting PSD follows a flatter slope, with $\alpha = 2.4$. In order that the resulting PSD not be biased, the observational data length must be longer than 100 times the break timescale.

These studies suggest that the NPSDs derived in this paper may also be biased, and the actual slopes may be *steeper* than we have estimated. In fact, the steep PSD could be the result of red-noise leak even if variability shorter than the characteristic timescale is really absent. On the other hand, it might be explained by the superposition of rapid *microflares* (e.g., less than 10% fluctuations) that are hidden behind large flares occurring on a timescale of the order of 1 day or longer (factor of $\sim 2$). At present, we cannot discriminate between these situations. Time series analysis with much better photon statistics as well as more detailed simulations would clarify this point. Work along these lines is now in progress (Tanihata et al. 2001) but is beyond the scope of this paper.

### 3.2. *Seyfert Galaxies versus Blazars*

Comparing our results with those of other black hole systems is quite interesting, as it is well known that the PSDs of Seyfert galaxies and Galactic black holes in the X-ray band also behave as power laws over some temporal frequency range. Our results (Tables 3 and 4) are contrasted with those of Hayashida et al. (1998) in Figure 7. We note that Hayashida et al. (1998) fit the NPSD with a single power law in the frequency range $f \geq 10^{-5}$ Hz. Lower frequency data were not available because a typical *Ginga* observation lasted only 1 day, with longer data sets containing large gaps. The situation is similar for the typical *ASCA* and *RXTE* observations, but not for the three long-look observations. These data lower the frequency limit to $10^{-6}$ Hz (Figs. 3*c*, 3*d*, and 3*g*). To make a quantitative comparison with Hayashida et al. (1998), we thus measured the PSD slope from a power-law fit in the frequency range $f \geq 10^{-5}$ Hz; these are $2.14 \pm 0.06$, $2.92 \pm 0.27$, and $2.23 \pm 0.10$, respectively, for the cases of Mrk 421, Mrk 501, and PKS 2155−304 ($\alpha$ of Table 4).

We find that the PSD slopes of the TeV sources are clearly different from those of Seyfert galaxies and Galactic black holes, on timescales shorter than 1 day. Quasi-fractal behavior ($1 < \alpha < 2$) is a general characteristic of Seyfert galaxies and Galactic black holes, while the power-law indices are steeper for the TeV-emitting sources ($2 < \alpha < 3$). This presumably reflects the different physical origins of and/or locations for the X-ray production. In fact, Seyfert galaxies and Galactic black holes are believed to emit X-ray photons nearly isotropically from the innermost parts of the

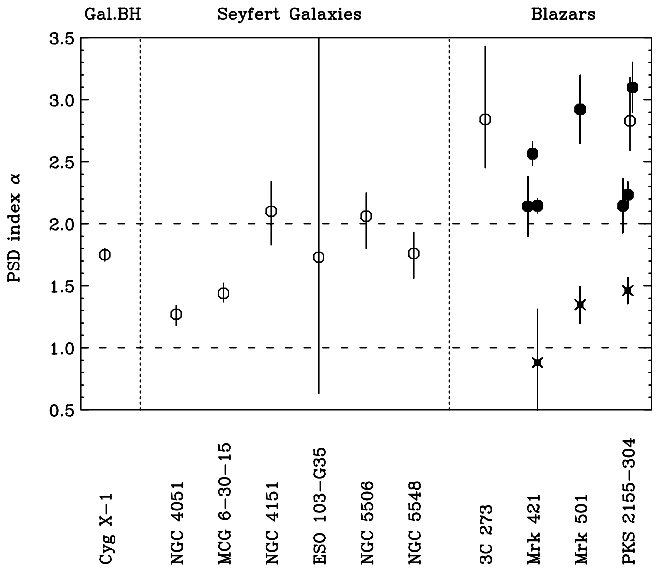


FIG. 7.—Comparison of PSD slopes for various black hole systems. *Open circles*: Hayashida et al. (1998). *Filled circles*: PSD slope $\alpha$ determined from a *single*–power-law fit (Tables 3 and 4; this work). To make quantitative comparison with Hayashida et al. (1998), we limit the fitting range to $10^{-5}$ Hz $\leq f \leq 10^{-3}$ Hz. Full details are given in the text. *Crosses*: PSD slope $\alpha_L$ in the *low*-frequency range determined from a *broken* power-law fit (Table 4; this work).

accretion disk (see, e.g., Tanaka et al. 1995; Dotani et al. 1997), while nonthermal emission from a relativistically beamed jet is the most likely origin of X-rays for blazar-like sources (see § 1).

We note that Hayashida et al. (1998) have estimated black hole masses in various types of AGNs using time variability. A linear proportionality between the variability timescale and the black hole mass was assumed, and this relation for Cyg X-1 ($M \simeq 10\ M_{\odot}$) was used as a reference point. Such an approach may be viable for AGNs for which the emission mechanisms are thought to be similar to Galactic black hole systems (e.g., Seyfert galaxies), but not for the blazar class. Indeed, the masses derived by their method for the blazars 3C 273 and PKS 2155−304 indicated that the observed bolometric luminosity exceeds the Eddington limit; this can be interpreted as indicating the importance of beaming effects in these objects. To estimate the mass of the central engine postulated to exist in blazars, a completely different approach must be applied, as discussed below.

### 3.3. *Implication for the Mass of the Central Engine*

As first pointed out by Kataoka (2000), the little power of rapid variability ($\leq 1$ day) in TeV sources provides important clues to the X-ray–emitting site in the jet. The characteristic timescale of each flare event $t_{\rm var} \geq 1$ day should reflect the size of the emission region (see below), which we infer to be $\geq 10^{16}(\Gamma/10)$ cm in the source comoving frame, if emitting blobs are approaching with Lorentz factors $\Gamma$ ($\Gamma \simeq 10$; Vermeulen & Cohen 1994). This range of Lorentz factors is independently inferred from constraints that can be derived from the spectral shape and variability of TeV blazars (e.g., Tavecchio, Maraschi, & Ghisellini 1998; Kataoka et al. 1999).

If the jet is collimated to within a cone of constant opening angle $\theta \simeq 1/\Gamma$ and the line-of-sight extent of shock is comparable with the angular extent of the jet, one expects that the X-ray emission site is located at distances $D \geq 10^{17}(\Gamma/10)^2$ cm from the base of the jet. Only little variability shorter than $t_{\rm var}$ strongly suggests that no significant X-ray emission can occur in regions closer than this to the black hole. The relativistic electrons responsible for the X-ray emission are most likely accelerated and injected at shock fronts occurring in the jet (e.g., Inoue & Takahara 1996; Kirk et al. 1998; Kusunose et al. 2000). The lack of short-term variability may then imply that shocks are nearly absent until distances of $D \geq 10^{17}(\Gamma/10)^2$ cm. Two different ideas have been put forward as to how and where shocks form and develop in blazar jets: external shocks and internal shocks. Both have also been extensively discussed in relation to $\gamma$-ray bursts.

Dermer & Chiang (1998; see also Dermer 1999) have proposed an *external shock* model, wherein the shocks arise when outflowing jet plasma decelerates upon interaction with dense gas clouds originating outside the jet. The precise nature of the required gas clouds is uncertain, but they may be similar to the ones postulated to emit the broad emission lines in Seyfert galaxies and quasars. It is interesting to note that the location of the broad-line regions in such strong emission-line objects have been inferred to be $10^{17-18}$ cm from the nucleus (e.g., Ulrich et al. 1997), in line with the distances presented above. It remains to be seen whether this picture is viable for the BL Lac objects considered here; gas clouds may be more dilute or absent in such objects as suggested by the weakness of their emission lines (e.g., Böttcher & Dermer 1998 and references therein). However, this could instead be due to a weaker central ionizing source rather than a difference in gas cloud properties.

An alternative view concerns *internal shocks*, originally invoked to explain the optical knots in the jet of M87 (Rees 1978). Ghisellini (1999, 2001) has pointed out that this idea successfully explains some observed properties of blazars. In this scenario, it is assumed that the central engine of an AGN intermittently expels blobs of material with varying bulk Lorentz factors rather than operating in a stationary manner.

Consider, for simplicity, two relativistic blobs with bulk Lorentz factors $\Gamma$ and $a_0\Gamma$ ($a_0 > 1$) ejected at times $t = 0$ and $t = \tau_0 > 0$, respectively. The second, faster blob will eventually catch up and collide with the first, slower blob, leading to shock formation and generation of a corresponding X-ray (and possibly TeV) flare. (A more realistic situation would envision sequential ejections of many blobs, inducing multiple collisions and a series of flares; e.g., Fig. 1*c*). The time interval between the two ejections is determined by the variability of the central engine and is expected to be at least of the order of the dynamical time close to the black hole, i.e., approximately the Schwarzschild radius ($R_g$) light-crossing time. Writing $\tau_0 = kR_g/c$, where $k \geq 3$, the distance $D$ at which the two blobs collide is

$$D = c\tau_0\,\Gamma^2\,\frac{2a_0^2}{a_0^2-1} = 10^3\,\frac{k}{10}\left(\frac{\Gamma}{10}\right)^2\frac{2a_0^2}{a_0^2-1}\,R_g\,. \qquad (3)$$

The radius of the jet at $D$ is

$$R = D\sin\theta \simeq D\theta \simeq D/\Gamma\,, \qquad (4)$$

which is taken to be equal to the emission blob size. Accounting for time shortening by a factor $\simeq 1/\Gamma$ due to beaming, the observed variability timescale should be

$$t_{\rm var} \simeq \frac{D}{c\Gamma^2} = 10\,\frac{k}{10}\,\frac{2a_0^2}{a_0^2-1}\,\frac{R_g}{c}\,. \quad (5)$$

Substantial dissipation and radiation of the jet kinetic energy will not take place until the blobs collide, and this can only occur above a minimum distance $D$, delimited by the minimum value of $k$. It is then a natural consequence that variability on timescales shorter than a certain value ($D/c\Gamma^2$) is suppressed, as indicated from the temporal studies presented in this paper.

It is apparent in equation (5) that the minimum variability timescale depends on the mass of the central black hole. Taking the typical observed value, we obtain

$$M \simeq 9\times 10^8\,\frac{t_{\rm var}}{\rm day}\,\frac{10}{k}\,\frac{a_0^2-1}{2a_0^2}\,M_\odot\,. \quad (6)$$

In Figure 8, we plot the black hole mass $M$ as a function of $a_0$ for various parameter sets $k$ and $t_{\rm var}$. Even when assuming a wide range of parameters ($k = 5$, 20, and 100 and $t_{\rm var}$/day = 1 and 10), the mass of the central black hole is well constrained to $10^7 < M/M_\odot < 10^{10}$.

The discussion presented above is based on the assumption that the characteristic timescale of X-ray variability is indicative of the size of the emission region $t_{\rm crs}$ ($=R/c$). On the other hand, one might imagine that this timescale also reflects the electron synchrotron cooling time ($t_{\rm cool}$), the electron acceleration timescale in the shock ($t_{\rm acc}$), and/or the timescale over which the accelerated electrons are injected into the emission region. In general terms, this is true, but we believe that relaxation of local variability by light-travel–time effects inside the emitting blob must be the dominant effect, particularly in the X-ray band.

For example, Kataoka et al. (2000) discovered that the duration of a flare observed in PKS 2155−304 (Fig. 1*f*) is the *same* in different X-ray energy bands, which is at odds with a picture in which the rise time and decay time of the flare are *directly* associated with $t_{\rm acc}$ and $t_{\rm cool}$, respectively,

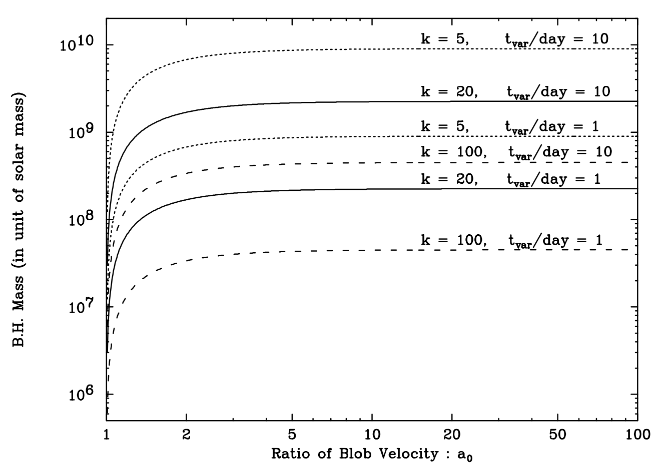


FIG. 8.—Black hole mass $M$ plotted as a function of $a_0$, where $a_0$ is the ratio of velocity of blob 1 and blob 2 (see text for more details). The mass was estimated for various parameter sets: $k = 5$, 20, and 100 and $t_{\rm var}$/day = 1 and 10.

both of which should be energy dependent. Furthermore, they found that $t_{\rm cool}$ ($\simeq t_{\rm acc}$ at the highest electron energy) for the X-ray–emitting electrons is much shorter than $t_{\rm crs}$, resulting in the quasi-symmetric flare light curves often observed in these TeV sources (e.g., Figs. 1*c* and 1*f*). Taking into account the fact that rapid variability faster than $t_{\rm var}$ is suppressed (Fig. 3), the $t_{\rm var}$ of TeV blazars is most probably characterized by $R/c$.

We also note that extremely rapid variability on subhour timescales has sometimes been observed for Mrk 421 and Mrk 501 in TeV $\gamma$-rays (Gaidos et al. 1996; Quinn et al. 1999) and more recently in X-rays as well (Catanese & Sambruna 2000). These types of events, which may be relatively rare, could perhaps be interpreted as shocks forming with strongly anisotropic geometries, albeit with a low duty cycle. If the line-of-sight extent of the shock $d$ was much thinner than the angular extent of the jet $R$, the observed timescale could be $\sim d/c$ rather than $R/c$ (e.g., Salvati, Spada, & Pacini 1998).

At the opposite end of the spectrum, our temporal studies show that the SFs of TeV blazars continue to *increase* with flatter slopes on longer timescales ($t \geq 1/f_{\rm br}$; Fig. 5). This means that in addition to the day-timescale flares, the TeV sources manifest variations in the baseline component. Such long-term variability may possibly be associated with that occurring in the accretion disk, e.g., various instabilities of the disk, or changes in the accretion rate. As the putative launching site of the jet, the accretion disk should inevitably exert a strong influence and could significantly modulate the process of jet plasma ejection. It is noteworthy that the time profiles of TeV blazars become more similar to those of Seyfert galaxies and Galactic black holes for timescales longer than $\sim$1 day.

## 4. CONCLUSIONS

We have studied the X-ray variability of three TeV $\gamma$-ray sources, Mrk 421, Mrk 501, and PKS 2155−304, in the widest time domain possible, from $10^3$ to $10^8$ s. Our analyses show clear evidence for a rollover with a timescale of order or longer than 1 day, both in the power spectra and the structure functions. Importantly, these rollovers can be interpreted as the characteristic timescale of successive flare events. We discovered that below this timescale, there is only small power in the variability, as indicated by steep PSDs of $f^{-2\sim-3}$. This is very different from other types of mass-accreting systems, for which the variabilities are well represented by a fractal nature. Our results suggest that the X-rays are *not* generated throughout the jet but are *preferentially* radiated from distances of $D \geq 10^{17}$ cm from the jet base, if emission blobs have bulk Lorentz factors $\Gamma \simeq 10$. As a possible interpretation of the variability in TeV blazars, the internal shock scenario was discussed. The observational properties can be consistently explained if the masses of the central black holes are $M \simeq 10^{7-10}\,M_\odot$ and the shocks start to develop at $D \geq 10^2 R_g$. Similar temporal studies at different wavelengths, from radio to $\gamma$-rays, as well as for different classes of blazars, will be valuable to discriminate between various emission models for blazars, as well as to provide important clues to the dynamics of jets.

We greatly appreciate an anonymous referee for his/her helpful comments and suggestions to improve the manuscript. J. K. acknowledges a Fellowship of the Japan Society for Promotion of Science for Japanese Young Scientists.

REFERENCES

Angel, J. R. P., & Stockman, H. S. 1980, ARA&A, 18, 321
Böttcher, M., & Dermer, C. D. 1998, ApJ, 501, L51
Buckley, J. H., et al. 1996, ApJ, 472, L9
Burke, B. E., et al. 1991, Proc. IEEE, 38, 1069
Cagnoni, I., Papadakis, I. E., & Fruscione, A. 2001, ApJ, 546, 886
Catanese, M., et al. 1997, ApJ, 487, L143
Catanese, M., & Sambruna, R. M. 2000, ApJ, 534, L39
Chadwick, P. M., et al. 1999, ApJ, 513, 161
Chiang, J., et al. 2000, ApJ, 528, 292
Deeter, J. E., & Boynton, P. E. 1982, ApJ, 261, 337
Dermer, C. D. 1999, Astropart. Phys., 11, 1
Dermer, C. D., & Chiang, J. 1998, NewA, 3, 157
Done, C., Madejski, G. M., Mushotzky, R. F., Turner, T. J., Koyama, K., & Kunieda, H. 1992, ApJ, 400, 138
Dotani, T., et al. 1997, ApJ, 485, L87
Edelson, R., & Nandra, K. 1999, ApJ, 514, 682
Gaidos, J. A., et al. 1996, Nature, 383, 319
Ghisellini, G. 1999, Astron. Nachr., 320, 232
———. 2001, ASP Conf. Ser. 227, Blazar Demographics and Physics, ed. P. Padovani & C. M. Urry (San Francisco: ASP), 85
Hartman, R. C., et al. 1999, ApJS, 123, 79
Hayashida, K., et al. 1998, ApJ, 500, 642
Heidt, J., & Wagner, S. J. 1996, A&A, 305, 42
Hughes, P. A., Aller, H. D., & Aller, M. F. 1992, ApJ, 396, 469
Inoue, S., & Takahara, F. 1996, ApJ, 463, 555
Iyomoto, N. 1999, Ph.D. thesis, Univ. Tokyo
Iyomoto, N., & Makishima, K. 2001, MNRAS, 321, 767
Jahoda, K., et al. 1996, Proc. SPIE, 2808, 59
Kataoka, J. 2000, Ph.D. thesis, Univ. Tokyo
Kataoka, J., et al. 1999, ApJ, 514, 138
———. 2000, ApJ, 528, 243
Kawaguchi, T., et al. 2000, PASJ, 52, L1
Kirk, J. G., Rieger, F. M., & Mastichiadis, A. 1998, A&A, 333, 452
Kusunose, M., Takahara, F., & Li, H. 2000, ApJ, 536, 299
Lamer, G., & Wagner, S. J. 1998, A&A, 331, L13
Macomb, D. J., et al. 1995, ApJ, 449, L99 (erratum 459, L111 [1996])
Makishima, K., et al. 1996, PASJ, 48, 171
Nandra, K., et al. 1997, ApJ, 476, 70
Nowak, M. A., & Chiang, J. 2000, ApJ, 531, L13
Ohashi, T., et al. 1996, PASJ, 48, 157
Paltani, S., et al. 1997, A&A, 327, 539
Papadakis, I. E., & Lawrence, A. 1995, MNRAS, 272, 161
Pian, E., et al. 1998, ApJ, 492, L17
Punch, M., et al. 1992, Nature, 358, 477
Quinn, J., et al. 1996, ApJ, 456, L83
———. 1999, ApJ, 518, 693
Rees, M. J. 1978, MNRAS, 184, 61P
Salvati, M., Spada, M., & Pacini, F. 1998, ApJ, 495, L19
Simonetti, J. H., Cordes, J. M., & Heeschen, D. S. 1985, ApJ, 296, 46
Tagliaferri, G., et al. 1991, ApJ, 380, 78
Takahashi, T., et al. 1996, ApJ, 470, L89
———. 2000, ApJ, 542, L105
Takahashi, T., Madejski, G., & Kubo, H. 1999, Astropart. Phys., 11, 177
Tanaka, Y., et al. 1995, Nature, 375, 659
Tanihata, C., Urry, C. M., Takahashi, T., Kataoka, J., Wagner, S. J., Madejski, G. M., Tashiro, M., & Kouda, M. 2001, ApJ, submitted
Tavecchio, F., Maraschi, L., & Ghisellini, G. 1998, ApJ, 509, 608
Thompson, D. J., et al. 1993, ApJS, 86, 629
Timmer, J., & König, M. 1995, A&A, 300, 707
Ulrich, M.-H., Maraschi, L., & Urry, C. M. 1997, ARA&A, 35, 445
Urry, C. M., & Padovani, P. 1995, PASP, 107, 803
Vermeulen, R. C., & Cohen, M. H. 1994, ApJ, 430, 467
von Montigny, C., et al. 1995, ApJ, 440, 525
Wagner, S. J., & Witzel, A. 1995, ARA&A, 33, 163
Yamashita, A., et al. 1997, Proc. IEEE, 44, 847
Zhang, Y. H., et al. 1999, ApJ, 527, 719